Influence of delocalized states on electron scattering by carbon nanotubes under various configurations

Ch. Adessi, M. Devel, and J.-M. Vigoureux
Laboratoire de Physique Moléculaire, UMR CNRS 6624, 16 route de Gray, F-25030 Besançon CEDEX, France
(Received 8 March 2000)

In the family of electron projection microscopes, the Fresnel projection microscope (FPM) allows observation in direct space of small organic fibers such as carbon nanotubes, with electron energies about 200 eV. With carbon nanotube material the optical Fresnel theory fails to explain all the features observed experimentally. We have performed simulations of FPM images of carbon nanotubes by combining quantum-mechanical electron diffusion theory with an *ab initio* method to include the properties of the molecular object. Simulations done with a (5,5) nanotube do reproduce the experimental occurrence of a very bright and contrasted geometrical projection of thin fibers, the so-called ''sucking-in'' effect. Furthermore, they allow to link this phenomenon with the large spreading of the effective potential occurring with nanotubes. Patterns in the simulated images of multiwall carbon nanotubes and ropes of nanotubes are reported. They are mainly governed by interferences occurring between the scattered waves coming from the different nanotubes. Ropes lead to large fringes unlike multiwall nanotubes, which lead to constructive interferences between the scattered waves. This constructive behavior is pointed out by means of a chiral inner nanotube, which leads to specific longitudinal fringes and an asymmetric pattern of the images as it is also reported for single-wall chiral nanotubes.

I. INTRODUCTION

Since they have been discovered,[1] carbon nanotubes have rapidly revealed surprising electronic properties such as their metallic or semiconducting behavior.[2] One implication of this property, is the possible use of nanotubes as molecular transistors[3,4] or nanoscale devices.[5–8] Moreover, quantized energy levels have been observed with short nanotubes in scanning tunneling microscopy[9] and theoretically interpreted as levels in a one-dimensional quantum box.[10] These properties clearly came from the low-energy electrons of the material. It is then not very surprising that microscopies,[11–15] which use electrons with energies about 200 eV, have revealed typical interactions between the electronic beam and carbon nanotubes. These interactions lead to phenomena such as the sucking of the incident beam inside the geometrical projection of the nanotubes.[16]

For the last decade, electron projection microscopies such as the Fresnel projection microscope (FPM),[15] have enjoyed a renewal of interest thanks to the development of metallic field emitters allowing electronic emission from the last atom of a tip apex, with a very small energetic spread ($\simeq$0.1 eV) for a typical energy of 200 eV and a small opening angle (half-opening about 5°).[17] These properties allow the observation of nanometer size objects with a resolution of about 0.5 nm. The observations of small diameter nanofibers such as carbon fibers[16] or carbon nanotubes,[18] have revealed phenomena that cannot be simply interpreted by means of an optical model,[19] i.e., which do not come from the Fresnel diffraction patterns of a thread or of a slit. The first effect of this type simulated here and observed experimentally with nanotubes, is the occurrence of the so-called ''sucking-in'' phenomenon for which the fiber appears bright with a very high contrast with respect to the incident beam. Other interesting effects allow us to discuss the opportunity to differentiate the specific FPM signatures of single-wall, multiwall, and ropes of nanotubes. Finally, we have studied the possibility of using the experimental observation of some longitudinal periodicity inside the geometrical projection of nanotubes to recover a specific periodic structure of the nanotube. For that purpose, we have performed quantum simulations of images of carbon nanotubes in different conformations (ropes, multiwall, chiral, and achiral single wall).

The methodology used to simulate FPM images of carbon nanotubes, corresponds to an integral reformulation of the time-independent Schrödinger equation in order to compute the wave function of an electron emitted from a point source and scattered by a molecule.[20] In this context, the time-independent approximation is justified by the high stability of the electronic beam. The point-source representation of the electronic source is satisfactory with regard to the small dimension of the emitting region, which is about 0.5 Å.[17] The typical energy of the emitted electrons ranges from 100 to 200 eV. Inelastic scattering, as observed in electron-energy-loss spectroscopy[21] with carbon nanotubes and occurring at energies above 300 eV, is in this context negligible. On the other hand, for this energy, multiple diffusion processes are not negligible compared with single one's. Thus, with the aim of simulating FPM images, we have combined a scattering formalism with an *ab initio* method to take into account multiple diffusion processes. This has been practically done by means of an atomic-orbital expansion of the electronic states of the nanotube. This technique allows us to describe efficiently the valence electrons of nanotubes with typically 600 atoms, hence to simulate multiwall and ropes of nanotubes.

In the next section, we summarize the scattering formalism and the *ab initio* method used to simulate FPM images. Then, simulated images of nanotubes are presented: First the

sucking-in phenomenon is discussed on the basis of a series of simulated images of a (5,5) nanotube for increasing distances with respect to the beam center; then, the patterns shown on simulated images of single-wall, multiwall, and ropes of nanotubes are compared and discussed; finally, the occurrence of periodic structures over FPM images is discussed.

II. RESOLUTION METHOD

A. Overview

With the aim of simulating FPM images of carbon nanotubes, the time-independent Schrödinger equation is recast into an integral form corresponding to the Lippmann-Schwinger (LS) equations.[22] The two formulations used here are the following:

$$\varphi(\vec{r}) = \varphi_0(\vec{r}) + \int d^3r'\, G_0(\vec{r},\vec{r}';E) V_{eff}(\vec{r}')\varphi(\vec{r}'), \quad (1)$$

$$\varphi(\vec{r}) = \varphi_0(\vec{r}) + \int d^3r'\, G(\vec{r},\vec{r}';E) V_{eff}(\vec{r}')\varphi_0(\vec{r}'), \quad (2)$$

where V_{eff} represents the effective potential of the one body Schrödinger equation associated with the carbon nanotube in vacuum, φ the scattered wave, φ_0 a spherical incident wave limited by a Gaussian envelope, $G_0(\vec{r},\vec{r}';E)$ the vacuum Green's function for a given energy E, and $G(\vec{r},\vec{r}';E)$ the Green's function of the full system.

The discretization of Eq. (1) in direct space gives rise to a system of N equations with N unknowns, allowing the calculation of the scattered wave in the whole space. This technique, already used successfully,[20] is limited by the number of discretization points. To circumvent this limitation, we have used a self-consistent field (SCF) method (for a review, see Ref. 23) to compute the Green's function $G(\vec{r},\vec{r}';E)$. This allows us to compute the scattered wave by means of Eq. (2) and to propagate it at any point in space by means of Eq. (1). The inherent limitation is then no more born by the number of discretization points but by the ability to compute the Green's function $G(\vec{r},\vec{r}';E)$. Theoretically, one could use the spectral representation of G:

$$G(\vec{r},\vec{r}';E) = \sum_{i=1}^{\infty} \frac{\psi_i(\vec{r})\psi_i^*(\vec{r}')}{E-\epsilon_i}, \quad (3)$$

where $\psi_i(\vec{r})$ represents any electronic state of the molecule and ϵ_i its corresponding eigenvalue. Thus, the summation should in fact be a real summation over the discrete spectrum and an integral one over the continuum states. However, for computational reasons, this summation is truncated to a finite number of occupied and unoccupied discrete states, computed by expansion over a finite basis. This approximation is coherent with the fact that the influence of the incident electron on the molecular states has been neglected. This is justified by the facts that the energy of the incident electron is much greater than the energies of the valence electrons. Furthermore, no resonance effect has experimentally been seen in FPM, whereas results from Mayer *et al.*[24] have shown, in the case of a C_{60} molecule, that the influence of the dynamical polarizability of C_{60} is only noticeable near a plasmon resonance. Hence, in this formalism, the self-consistency of the problem is no more contained in the LS equation but in the determination of the electronic states of the molecule.

B. Self-consistent field method

The main equation of the SCF method is the one body Schrödinger equation, which can be expressed as

$$\left[-\frac{\hbar^2}{2m}\vec{\nabla}_r^2 + V_{eff}(\vec{r}) \right] \psi_i(\vec{r}) = \epsilon_i \psi_i(\vec{r}), \quad (4)$$

with $V_{eff}(\vec{r}) = v_{ext}(\vec{r}) + v_{Hart}(\vec{r}) + v_{xc}[\rho(\vec{r})]$, where v_{ext} represents the core potential of the atoms, v_{Hart} the Colombian repulsion between electrons, and v_{xc} the exchange-correlation potential expressed in terms of a functional of the electronic density (corresponding to:

$$\rho(\vec{r}) = \sum_{i=1}^{N_{el}} \psi_i^*(\vec{r})\psi_i(\vec{r}),$$

where N_{el} is the number of electrons of the molecule). To solve Eq. (4), an expansion of the electronic states over a finite basis is used, leading to an eigenvalue equation. Starting from an initial set for the expansion of the electronic states, an effective potential is then deduced and used to solve the eigenvalue equation, leading to a new set and so on until convergency has been reached. The eigenvalue equation can be expressed as $\mathcal{H}\mathcal{C}_i = \epsilon_i \mathcal{S}\mathcal{C}_i$, where $\mathcal{H}$ represents the Hamiltonian matrix, $\mathcal{S}$ the overlapping matrix of the basis elements, $\mathcal{C}_i$ one eigenvector, and ϵ_i the corresponding eigenvalue. We used Slater's atomic orbitals[25] as a basis because interpretation of the diffusion calculation is easier when the truncation of the electronic expansion is modified. Its main disadvantage, compared to a Gaussian type basis, is the nonanalycity of the integrals involved in the Hamiltonian matrix elements calculation.

The external potential is expressed by means of a pseudopotential technique,[26] which allows to reduce the number of electrons involved in the eigenvalue equation. With this technique, the valence and the core electrons are dissociated with the assumption that the wave functions of the core electrons are weakly affected by their surrounding environment. This allows to include them in the Hamiltonian as a constant parametrized potential. The Hartree potential is described as

$$v_{\mathrm{Hart}}(\boldsymbol{r}) = \frac{e^2}{4\pi\epsilon_0} \int d^3r' \frac{\rho(\boldsymbol{r}')}{|\boldsymbol{r}-\boldsymbol{r}'|}.$$

Finally, the exchange-correlation potential comes from the local-density approximation. It corresponds to the formulation proposed by Ceperly and Alder[27] and parametrized by Perdew and Zunger.[28]

In order to consider molecules with typically 600 atoms, it is necessary to use some level of approximation in the resolution of the eigenvalue equation. A crude one consists in neglecting all three center integrals, since they are the most time consuming to compute. A softer one consists in neglecting those which do not involve nearest neighbors. These two levels of approximation have been used successively. In a first step, electronic states have been expanded over only one

atomic site excluding all three center integrals. After convergence, the configuration obtained with this approximation corresponds to electronic states localized on one atom. In order to include in the Green's function the collective properties due to the delocalized states (which lead for carbon nanotubes to metallic[2] or semiconductor properties), it is necessary to expand electronic states at least between nearest-neighbors atoms. This has been done in a last step where Hamiltonian and overlapping elements involving nearest-neighbor atoms were computed. This last step was the most time consuming due to the computational difficulties arising from the three center integrals that were calculated using spheroidal coordinates.

In all the presented results a $\{2s,2p,3s,3p\}$ basis was used. The inclusion of the $3s$ and $3p$ orbitals allows a satisfactory description of σ and π bonds for diffusion calculation. This inclusion is necessary in this formalism in order to include antibonding states in the Green's function of the system. Moreover, it will be pointed out that the use of a $\{2s,2p\}$ basis does not allow to recover the ''sucking-in'' effect. Tests of convergence were carried out for a C_{100} molecule: the same picture was simulated using a $\{2s,2p,3s,3p\}$ and $\{2s,2p,3s,3p,4s,4p\}$ basis. Even in logarithmic scale, differences on the pictures are barely noticeable. However, differences of the order of 15% can be noted on the maximum value.

C. Scattering formalism

By inserting Eq. (3) into Eq. (2), the following equation is obtained:

$$\varphi(\vec{r}) = \varphi_0(\vec{r}) + \sum_{i=1}^{\infty} \frac{\psi_i(\vec{r})}{E-\epsilon_i} \int d^3r'\, \psi_i^*(\vec{r}')V_{eff}(\vec{r}')\varphi_0(\vec{r}'). \tag{5}$$

However, this last equation cannot be used directly to compute the scattered wave function φ far away from the molecule. This limitation arises from the truncation of the expansion of the electronic states, which does not allow to get the correct asymptotic behavior for the scattered wave, due to a lack of high-radial momentum. To go around this difficulty, it is necessary to compute the scattered wave first in the source region (i.e., the region where the effective potential is different from zero) by means of Eq. (5) and then to use Eq. (1) to propagate this wave function far away from the molecule. This leads to:

$$\varphi(\vec{r}_{sc}) = \varphi_0(\vec{r}_{sc}) + \int d^3r\, G_0(\vec{r}_{sc},\vec{r};E)V_{eff}(\vec{r})\varphi_0(\vec{r}) + \sum_{i=1}^{\infty} \frac{A_i}{E-\epsilon_i} \int d^3r\, G_0(\vec{r}_{sc},\vec{r};E)V_{eff}(\vec{r})\psi_i(\vec{r}), \tag{6}$$

where sc refers to the screen position and $A_i = \int d^3r'\, \psi_i^*(\vec{r}')V_{eff}(\vec{r}')\varphi_0(\vec{r}')$. In this equation, the first integral term represents the Born approximation corresponding to a wave scattered only once by the molecule. The second integral term represents the remaining terms in the Born expansion, namely, the multiple diffusion processes corresponding to a wave scattered twice or more by the molecule. In this expansion of the scattered wave, the *i* subscript in the second integral term represents electronic states and not the order in the Born expansion. For such an expansion, in the context of electron projection microscopy, see Kreuzer *et al.*[29,30]

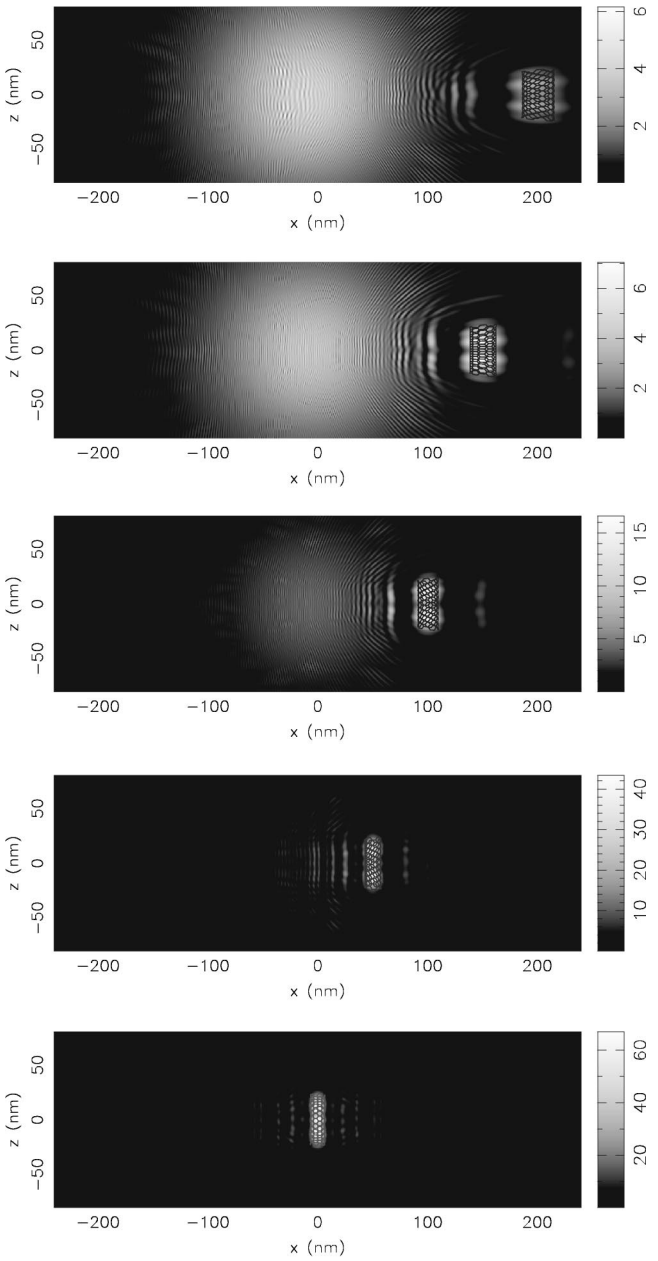

FIG. 1. Electron density of probability (in units of 10^{-7} nm^{-3}) on a screen 100 nm away from a (5,5) nanotube with 200 atoms, shifted in front of the electronic Gaussian beam. The source is 5 nm in front of the nanotube (for zero shift) and the electron energy is 150 eV. The shift value is ranging from 10 to 0 nm (top to bottom) by a step of 2.5 nm. The geometrical projection of the carbon skeleton has been superimposed on all the images.

III. NUMERICAL RESULTS

A. Simulation and interpretation of the sucking-in effect

FPM observation of some carbon fibers and some carbon nanotubes revealed very bright ''shadows'' without sur-

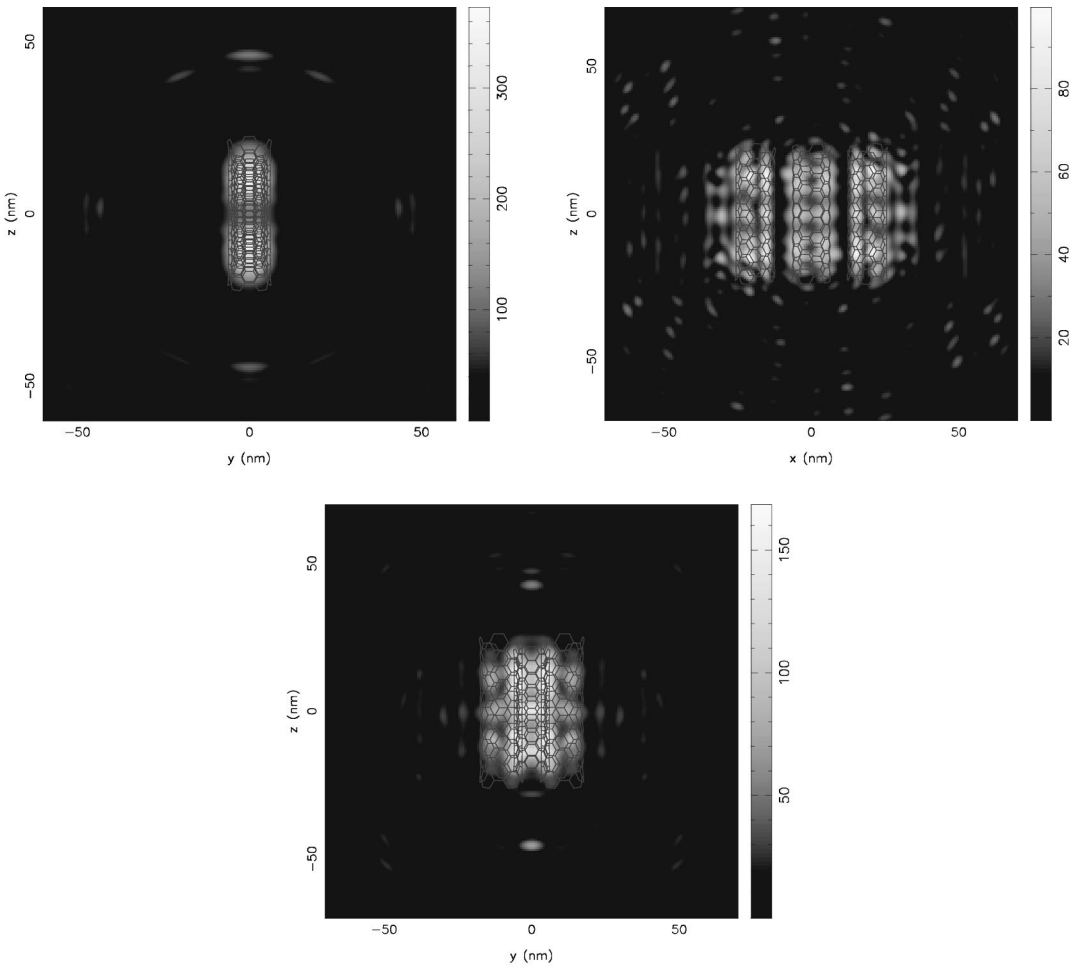

FIG. 2. Density of probability (in units of 10^{-7} nm^{-3}) on a screen 100 nm away from a linear rope of 3 (5,5) nanotubes. The axes of the nanotube are parallel and placed (see the text) one behind the other (left image), lined up in front of the source (central image) and in a triangular configuration (right image). The source is located 5 nm in front of the nearest nanotube and the electron energy is 150 eV.

rounding diffraction fringes, as if the beam was ''sucked'' by the molecule, hence the name ''sucking-in'' for this effect. Its experimental observation was initially done with carbon fibers,[16] but its intensity was greatly enhanced with carbon nanotubes. This phenomenon has been suspected to be linked with the thinness of the fibers. This hypothesis has been partly confirmed by simulations done with carbon fibers[31] and carbon nanotubes.[32] Other simulations with carbon fibers, done by Mayer and Vigneron,[33,34] have pointed out a large dependence of the phenomenon with the polarization of the fibers due to the applied field. In the case of carbon nanotubes modelled by using a linear combination of atomic orbitals with a $\{2s,2p\}$ basis,[20] a diameter dependence has been pointed out but no intensity enhancement has been observed. On the other hand, when using a $\{2s,2p,3s,3p\}$ basis, the phenomenon is fully recovered as reported on Fig. 1, where a (5,5) carbon nanotube is shifted in front of the electronic beam. For all these simulations, multiple diffusion processes are taken into account. Their influence is about one tenth of the amplitude of the single diffusion and they do not seem to play a part in the phenomenon.

As the nanotube gets nearer to the central axis of the beam, the width of the carbon skeleton projection is homothetically decreased. This phenomenon is also observable for the central diffraction fringe, thus emphasizing the projective hence real space nature of this microscopy. Moreover, for a large shift, only a small part of the total current is ''sucked'' into the shadow of the nanotube. Most of the emitted current does not suffer major perturbations and consequently, the Gaussian shape of the incident beam is observed. Conversely, the more the nanotube is brought closer to the axis of the beam, the more the emitted current is sucked into the shadow in agreement with experiment.[16] This phenomenon is clearly seen by comparing the maximum density of probability obtained in all these images. This comparison also reveals that the diffraction fringes are none the less always present. For the larger shifts, they are observable in the vicinity of the projected shadow, whereas for zero shift, they tend to disappear due to the very high intensity of the central fringe.

The addition of the $3s$ and $3p$ orbitals to the basis produces a noticeable change in the effective potential due to the larger spatial extension of the valence electrons. As the effective potential plays a dominant role in the integral part of the LS equation, this finally results in an intensity enhancement when compared to simulations for a $\{2s,2p\}$ basis. However, the position of the brightest fringes is not much affected. It is still governed by Fresnel diffraction: One gets a brighter central fringe for the smaller diameter, whereas two bright lateral fringes can be seen when the diameter is increased (see also Sec. III D).

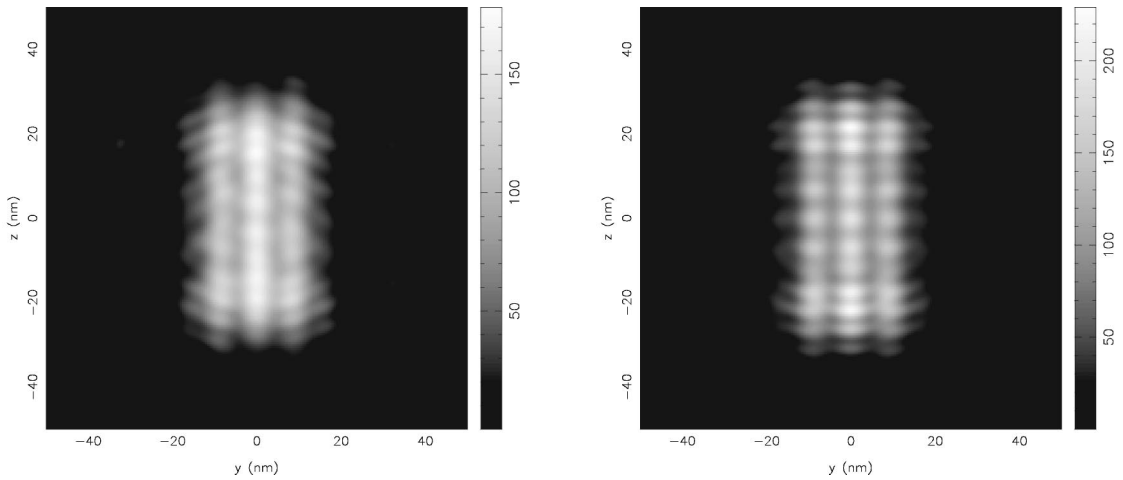

FIG. 3. Density of probability (in units of 10^{-7} nm^{-3}) on a screen 100 nm away from a double-wall nanotube constituted with a (10,10) outer layer and a (10,4) (left image) or (13,0) (right image) inner layer. The source is located 5 nm in front of the closest nanotube and the electron energy is 150 eV.

B. Ropes of (5,5) nanotubes

Experimentally, the single-wall nanotubes commonly used for the observation were produced by arc discharge and deposited on the transmission electron microscope grid in a drop of ethanol solution. According to high resolution transmission electron microscope (HRTEM) studies,[35] this procedure leads mostly to the formation of ropes of nanotubes. In order to differentiate the patterns of ropes with those of isolated nanotubes, we have simulated images of a rope of 3 (5,5) nanotubes (Fig. 2). Three configurations were used: Two correspond to a two-dimensional arrangement of the nanotubes, placed one behind the other along the axis of the electron beam for the left image, or side by side in a plane perpendicular to the electron beam for the central image; the last corresponds to a triangular arrangement (right image) of the axes of the tubes, which form a triangular prism perpendicular to the electron beam. In all these configurations, the distance between the axes of the nanotubes is 1.0 nm. For the left-hand side image (nanotubes behind one another), there is a great enhancement of the sucking-in phenomenon leading to a very high value of the density of probability. For the central image (nanotubes lined up in front of the source), the maximum of density of probability is about the same as the one obtained with an isolated (5,5) nanotube but interferences occur between the scattered waves coming from the different nanotubes, leading to diffraction fringes. These interferences inside the projected shadow of the rope do not allow to deduce the dimension of the rope from the location of these fringes unlike what is the case for a single fiber.[19] The triangular configuration (right image) is a mix of the two behaviors previously described. A relatively high-maximum value of the density of probability and the occurrence of diffraction fringes is found. Considering the low contrast between fringes, the experimental observation of such a structure would presumably be equivalent to the observation of a nanotube with a diameter smaller than the effective diameter of the triangular-shaped rope. Furthermore, the observation of an isolated nanotube with a diameter equal to that of the simulated rope (1.6 nm) would lead (see, for example, Fig. 5) to a projected shadow with a dark central fringe. In conclusion, the diameter that one can deduce from the size of a thin bright central diffraction fringe will be a good estimation if the observed nanotube is a single-wall one but not if it is a rope made of a few nanotubes.

C. Multiwall observation

Another configuration often encountered with carbon nanotubes is multiwall nanotubes. With the aim of pointing out specific patterns, we have simulated images of double-wall nanotubes constituted by a (10,10) overlayer and a (13,0) or (10,4) intralayer (Fig. 3). The other aim of these simulations was to investigate the impact of the internal structure on the images by means of the difference of chirality of the two internal nanotubes: The (13,0) is achiral whereas the (10,4) is chiral with a chiral angle of 16.1°. Furthermore, these two internal nanotubes have very close diameters. However, a close inspection of Fig. 3 reveals only one specific effect due to the chirality. This effect is a slight asymmetric pattern on the images of the (13,0) inside (10,10) multiwall, which expresses the chiral nature of the internal nanotube as it is reported with a single-wall nanotube (see Sec. III D). The other characteristic that can be pointed out from Fig. 3 is the nondestructive interference behavior of the different scattered waves. Actually, the scattered waves emitted by the internal tube and the external tube sum up without destructive interferences. This behavior differs from the one observed with ropes of nanotubes (see Sec. III B) for which destructive interferences occur between the scattered waves. Thus, the images of these peculiar carbon nanotubes with two walls present the characteristics of both layers. However, for a larger number of walls, the characteristics of the inner nanotubes would presumably be attenuated.

D. Chirality effect

Defects with dimensions less than the diffraction resolution cannot be resolved with FPM.[17,33] Thus, defects such as Stone–Wales defects corresponding to a pair of pentagon and heptagon for a nanotube, are not resolved with that microscope. Indeed, a simulation done with a (5,5) carbon nanotube presenting a Stone–Wales defect in its center gives no difference with the simulations presented in Fig. 1. Con-

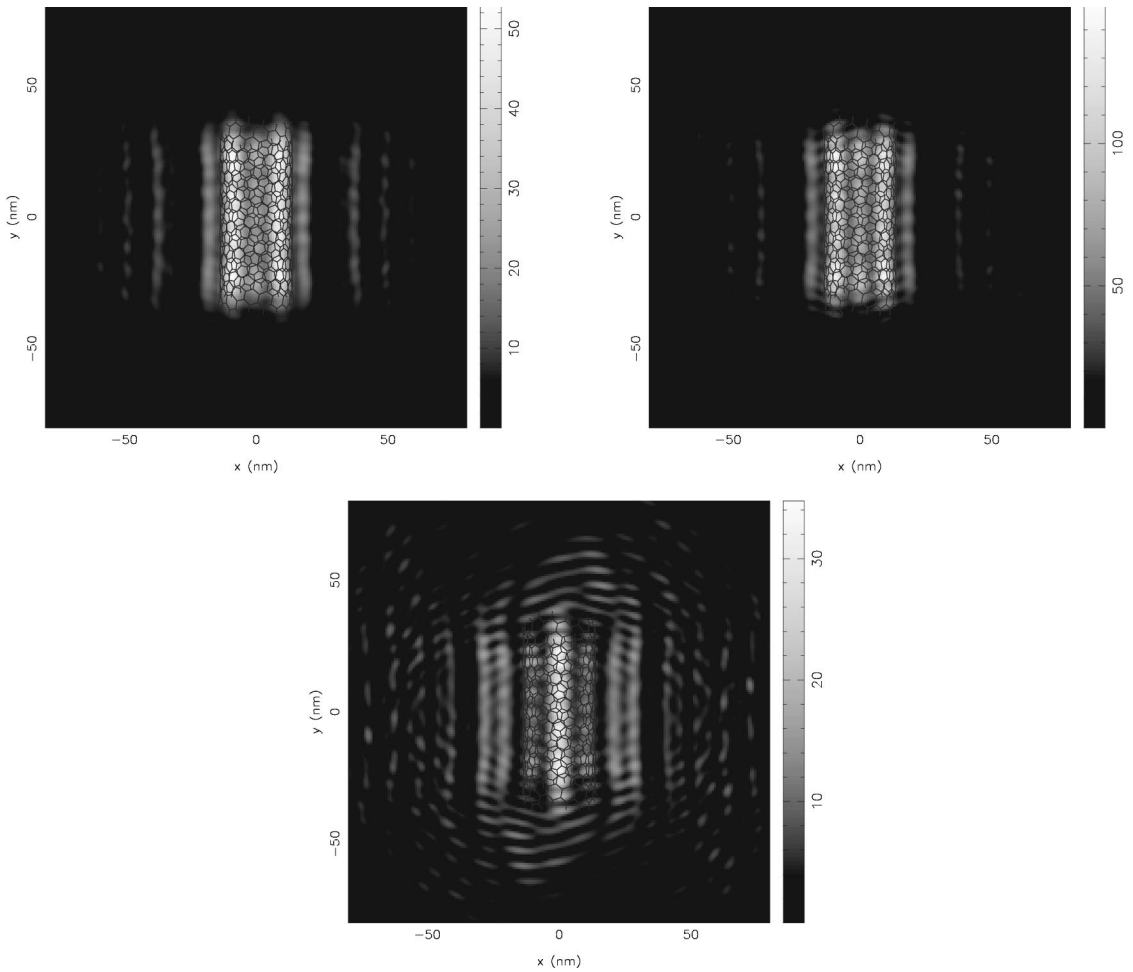

FIG. 4. Density of probability (in units of 10^{-7} nm^{-3}) on a screen 100 nm away from a (16,4) chiral nanotube with 608 atoms. The source is located 5 nm in front of the nanotube and the electron energy is 100 eV. From left to right: total scattered wave, first Born approximation, and multiple diffusion processes.

versely, periodic structures occurring in nanotubes are potentially observable due to the diffractive nature of the microscope. For instance, chiral nanotubes that have a large spatial period and a spiral symmetry, are expected to give rise both to real and reciprocal space phenomena. To assess the influence of chirality over FPM images, we show in Figs. 4 and 5 simulated images of two chiral nanotubes, namely, a (16,4) and a (20,5), both with a chiral angle of 10.89°. In order to estimate the different contributions of the single and multiple diffusion processes we have represented on these figures, the full (observed) density of probability and the contributions of the single and multiple diffusion processes. Comparing the full density of probability for the two nanotubes, we recover the typical behavior previously observed[20] when the diameter of the nanotube is increased. For the smaller diameter, the projected shadow of the nanotube is bright whereas it is darker for the larger diameter. This behavior is mainly governed by single diffusion processes due to their larger amplitude compared with multiple diffusion processes. One implication of the chirality is an asymmetric pattern (originating in the truncation of the helix at the two ends of the nanotube) which can be clearly seen on multiple diffusion process images. This pattern is also present in the full scattered wave images but less perceptible due to a largely dominant central fringe. This occurrence is due to the real-space nature of the imaging process of the microscope. Conversely, the periodic structure of the nanotube leads to longitudinal fringes and corresponds to a reciprocal space effect. Its dependence with the nanotube period can be clearly seen in Fig. 3. Moreover, the observed periodicity is at most about 1 nm (in the object plane) which is larger than the geometrical or the image acquisition resolution[17] of the microscope and so potentially observable experimentally.

IV. CONCLUSION

Simulated FPM images of carbon nanotubes with various configurations have been presented. These simulations were done by using a scattering formalism combined with an *ab initio* method. This allows to consider molecules with up to 600 atoms and to describe efficiently multiple diffusion processes occurring in the range of energy used in FPM.

In this framework, it is possible to recover the sucking-in phenomenon (which corresponds to a bright nanotube ''shadow'' with a high contrast). This has been achieved by means of a large basis for the electronic state expansion, which allow to recover the contrast enhancement thanks to the large spreading of the effective potential of the molecule, hence to the extension of delocalized states in nanotubes. However, the position of the diffraction fringes is still gov-

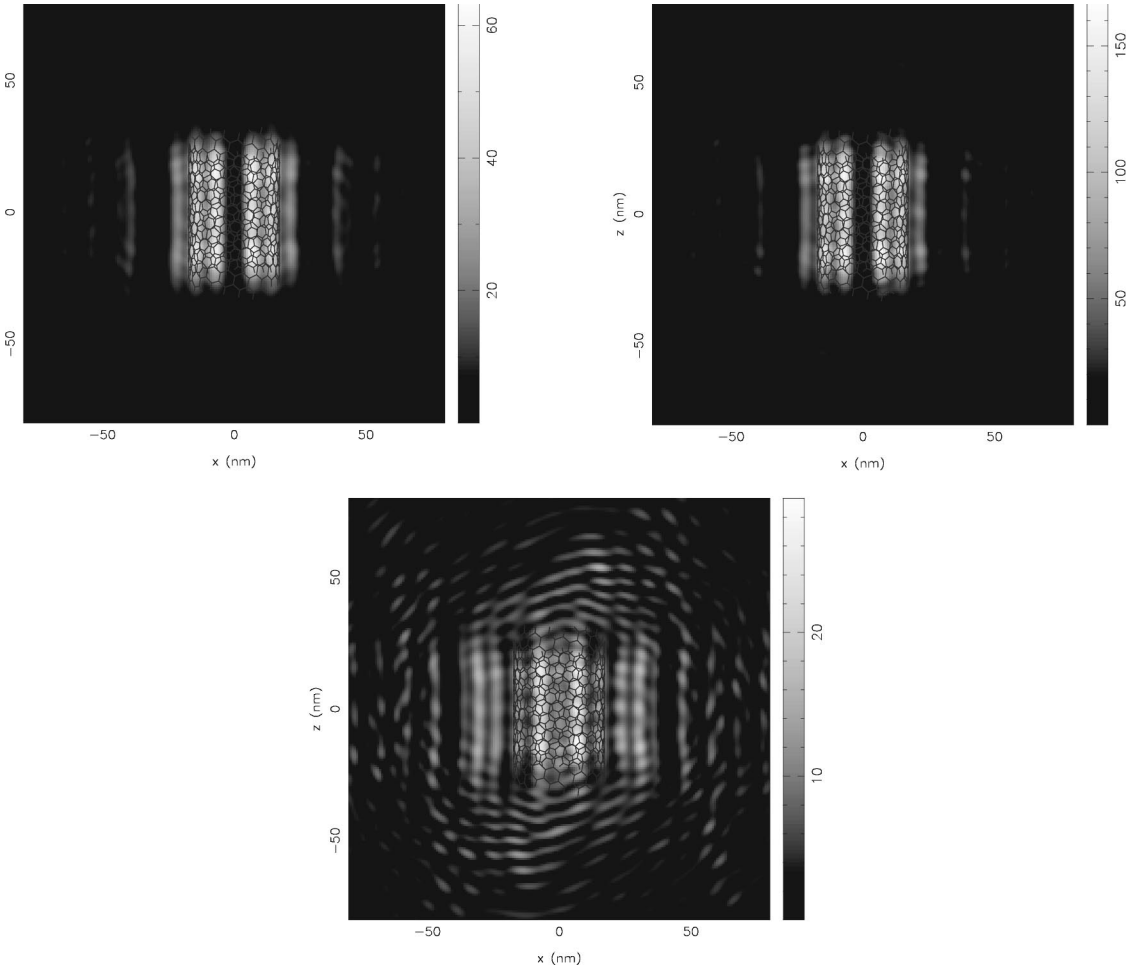

FIG. 5. Density of probability (in units of 10^{-7} nm^{-3}) on a screen 100 nm away from a (20,5) chiral nanotube with 620 atoms. The source is located 5 nm in front of the nanotube and the electron energy is 100 eV. From left to right: total scattered wave, first Born approximation, and multiple diffusion processes.

erned by Fresnel diffraction, allowing us to use the corresponding resolution criterium for diameter evaluation of thin single-wall nanotubes.

Simulations of systems composed with several nanotubes, such as ropes of nanotubes or multiwall nanotubes, have pointed out a large dependence of the images with the interferences occurring between the scattered waves coming from the different nanotubes. For a rope composed of three (5,5) nanotubes, large fringes inside the geometrical projection of the rope are observed for some configurations. This occurrence leads to the conclusion that it is not possible to deduce the diameter of the rope from the location of the first fringes contrary to what has been proven for a single fiber.[19] Conversely, for the double-wall nanotubes simulated here, no fringe is observed and the patterns of the two layers are present on the images. This has been pointed out by means of two distinct intralayers with the same diameter but different chirality.

Finally, simulated images of (20,5) and (16,4) nanotubes are reported showing that chiral nanotubes give rise to a slight asymmetric pattern observed in real space, originating from the ends of the tubes. Conversely, the occurrence of longitudinal fringes is due to the periodic structure of the nanotube and is observed in the reciprocal space. Moreover, this occurrence depends on the period of the nanotubes and is independent of the chiral nature of the nanotube (chiral or achiral).

ACKNOWLEDGMENTS

The authors gratefully acknowledge fruitful discussions with Ph. Lambin and P. Vincent. This work was performed under Contract Nos. 990028 and 9912160 with the CINES and IDRIS French national computing centers, respectively. One of the authors gratefully acknowledges the financial support of the GDR CNRS 1752 ''nanotubes.''

[1] S. Iijima, Nature (London) **354**, 56 (1991).
[2] J.W. Mintmire, B.I. Dunlap, and C.T. White, Phys. Rev. Lett. **68**, 631 (1992).
[3] S.J. Tans, M.H. Devoret, H. Tai, A. Thess, R.E. Smalley, L.J. Geerligs, and C. Dekker, Nature (London) **386**, 474 (1997).
[4] M. Bockrath, D.H. Cobden, P.L. Mceuen, N.G. Chopra, A. Zettl, A. Thess, and R.E. Smalley, Nature (London) **275**, 1922 (1997).
[5] L. Chico, V.H. Crespi, L.X. Benedict, S.G. Louie, and M.L. Cohen, Phys. Rev. Lett. **76**, 971 (1996).
[6] R.R. Saito, G. Dresselhaus, and M.S. Dresselhaus, Phys. Rev. B **53**, 2044 (1996).
[7] J.-C. Charlier, T.W. Ebbesen, and Ph. Lambin, Phys. Rev. B **53**, 11 108 (1996).
[8] M. Menon and D. Srivastava, Phys. Rev. Lett. **79**, 4453 (1997).
[9] L.C. Venema, J.W.G. Wildöer, S.J. Tans, J.W. Janssen, L.J. Hinne, L.J.T. Tuistra, L.P. Kouwenhoven, and C. Dekker, Science **283**, 52 (1999).
[10] A. Rubio, D. Sánchez-Portal, E. Artacho, P. Ordejón, and J.M. Soler, Phys. Rev. Lett. **82**, 3520 (1999).
[11] E.W. Muller, Ergeb. Exakten. Naturwiss. **27**, 290 (1953).
[12] A.J. Melmed, Appl. Phys. Lett. **12**, 100 (1968).
[13] A. Piquet, H. Roux, Vu Thien Binh, R. Uzan, and M. Drechsler, Rev. Phys. Appl. **6**, 105 (1971).
[14] H.-W. Fink, IBM J. Res. Dev. **30**(5), 460 (1986).
[15] Vu Thien Binh, V. Semet, and N. García, Appl. Phys. Lett. **65**, 2493 (1994).
[16] Vu Thien Binh and V. Semet, Ultramicroscopy **73**, 107 (1998).
[17] Vu Thien Binh, V. Semet, N. García, and L. Bitar, in *Optics at the Nanometer Scale: Imaging and Storing with Photonic Near Fields*, edited by M. Nieto-Vesperinas and N. García, Vol. 319 of NATO-ASI Ser.: E Applied Sciences (Kluwer Academic, Dordecht, 1996).
[18] Vu Thien Binh, P. Vincent, F. Feschet, and J.M. Bonard, Phys. Rev. B (to be published).
[19] Vu Thien Binh, V. Semet, and N. García, Ultramicroscopy **58**, 307 (1995).
[20] Ch. Adessi and M. Devel, Phys. Rev. A **60**, 2194 (1999).
[21] O. Stéphan, P.M. Ajayan, C. Colliex, F. Cyrot-Lackmann, and É Sandré, Phys. Rev. B **53**, 13 824 (1996).
[22] B.A. Lippmann and J. Schwinger, Phys. Rev. **79**, 469 (1950).
[23] F. Jensen, *Introduction to Computational Chemistry* (Wiley, Chichester, 1999).
[24] A. Mayer, P. Senet, and J.-P. Vigneron, J. Phys.: Condens. Matter **11**, 8617 (1999).
[25] J.C. Slater, Phys. Rev. **36**, 57 (1930).
[26] G.B. Bachelet, D.R. Hamann, and M. Schlüter, Phys. Rev. B **26**, 4199 (1982).
[27] D.M. Ceperly and B.J. Alder, Phys. Rev. Lett. **45**, 566 (1980).
[28] J.P. Perdew and A. Zunger, Phys. Rev. B **23**, 5048 (1981).
[29] H.J. Kreuzer, K. Nakamura, A. Wierzbicki, H.-W. Fink, and H. Schmid, Ultramicroscopy **45**, 381 (1992).
[30] H.-W. Fink, H. Schmid, H.J. Kreuzer, and A. Wierzbicki, Phys. Rev. Lett. **67**, 1543 (1991).
[31] A. Mayer and J.-P. Vigneron, Phys. Rev. B **56**, 12 599 (1997).
[32] Ch. Adessi, M. Devel, Vu Thien Binh, Ph. Lambin, and V. Meunier, Phys. Rev. B **61**, R13 385 (2000).
[33] A. Mayer and J.-P. Vigneron, Phys. Rev. B **60**, 2875 (1999).
[34] A. Mayer and J.-P. Vigneron, Ultramicroscopy **79**, 35 (1999).
[35] J.-M. Bonard, T. Stora, J.-P. Salvetat, J.-P. Maier, T. Stockli, C. Duschl, L. Forro, W.A. De Heer, and A. Chatelain, Adv. Mater. **9**, 827 (1997).